Reconstructing the bulk Fermi surface and superconducting gap properties from neutron scattering experiments

Tanmoy Das,[1,2] R. S. Markiewicz,[1] and A. Bansil[1]

[1]*Physics Department, Northeastern University, Boston, Massachusetts 02115, USA*
[2]*Theoretical Division, Los Alamos National Laboratory, Los Alamos, New Mexico 87545, USA*

We develop an analytical tool to extract bulk electronic properties of unconventional superconductors from inelastic neutron scattering spectra. We show that the upward and downward branches of the spin excitation spectra have distinct origins, with the upper branch representing a gapped spin-wave dispersion and the lower branch associated with Bogoliubov quasiparticle scattering on the Fermi surface. Combined, they produce an "hourglass" dispersion with 45° rotation of the spectrum, as found experimentally. The downward dispersion can be inverted to reveal the Fermi momentum dispersion of the single-particle spectrum as well as the corresponding superconducting (SC) gap function, analogously to the quasiparticle interference effect in scanning tunneling microscopy (STM). Whereas angle-resolved photoemission spectroscopy and STM provide surface-sensitive information, this inversion procedure provides bulk electronic properties. The technique is essentially model independent and can be applied to a wide variety of materials.

I. INTRODUCTION

The study of cuprate superconductivity has led to the discovery of a number of unexpected relationships between seemingly different spectroscopies. Scanning tunneling microscopy (STM) provides an outstanding example of this: While basically a real-space probe, it can extract momentum-space (k-space) information of the electronic Fermi surface and superconducting (SC) pairing symmetry usually associated with angle-resolved photoemission spectroscopy (ARPES). Elastic scattering of Cooper pairs leads to the quasiparticle interference (QPI) pattern measured by STM.[1,2] By analyzing the QPI pattern as a function of scattering angle (in q space) it is possible to reconstruct both band structure and gap information in k space. While the technique was originally developed for d-wave cuprates, it is finding wide applications in other materials, including pnictides, where the SC gap is probably of $s_\pm$ symmetry, and in non-superconducting topological insulators.

The development of a similar technique for inelastic neutron scattering (INS) has obvious advantages. First, ARPES and STM are surface-sensitive probes,[3,4] which in practice means that they can only be performed on materials that are readily cleaved. For the same reason, they are mainly restricted to quasi-two-dimensional materials, and the question always remains how sensitive the results are to surface effects, such as pinning, reconstruction, and excess scattering. In contrast, INS is a bulk probe which does not need special surface preparation and can readily be applied to three-dimensional materials. For instance, INS results on heavy-fermion materials were available years before the first high-resolution ARPES studies. Here we demonstrate that inelastic scattering between the particle and hole Bogoliubov quasiparticles generates a similar magnetic quasiparticle scattering (MQPS) profile which can be probed directly by INS measurements.[5–7] Taking all three spectroscopies together, we are able to establish a definite consistency between the r-space (STM), k-space (ARPES), and q-space (INS) dynamics of the unconventional Bogoliubov quasiparticles.

The overall phenomenology of neutron scattering in cuprates is well known, and a number of universal features have been experimentally identified[8–16] and theoretically interpreted.[5–7] The results indicate that a distinct low-energy magnetic mode is present near the antiferromagnetic nesting vector $\boldsymbol{Q} = (\pi,\pi)$ in almost all the cuprates. The intensity of this mode is enhanced in the SC state while its energy scales $\omega_{\mathrm{res}}(\boldsymbol{Q}) \propto 2\Delta_{\mathrm{SC}}$ for all cuprates,[17,18] suggesting a close connection of these modes with SC pairing. The dispersion of spectral weight away from this resonance peak also has a universal character, forming an "hourglass"-like pattern centered on the resonance mode and displaying a 45° rotation on passing through the resonance peak. Below the resonance energy, spectral weight disperses along the Cu-O bond direction, while above the resonance the dispersion peak lies along the diagonal direction. Despite an overall universality, many features of this "hourglass" dispersion are highly material specific and we show that the difference comes mainly from the nature of the pseudogap order among other band-structure-related properties.

This paper is organized as follows. In Sec. II, we introduce our inversion procedure and its analogy with the QPI pattern. The microscopic description of the magnetic resonance peak and its associated hourglass pattern is given in Sec. III. In this section, we have also used the experimental INS data and ARPES data to reconstruct one from the other. The constant-energy profile or the magnetic quasiparticle scattering pattern is given in Sec. IV, including the observation of several new **q** vectors away from $Q = (\pi,\pi)$, 45° rotation of the constant-energy profile, and direct comparison with QPI patterns. We discuss our results in the context of previous model calculations and conclude in Sec. V.

II. INVERSION PROCEDURE AND ITS ANALOGY WITH QPI PATTERN

Recalling the QPI pattern. We begin by describing the inversion procedure in INS, which is analogous to the common
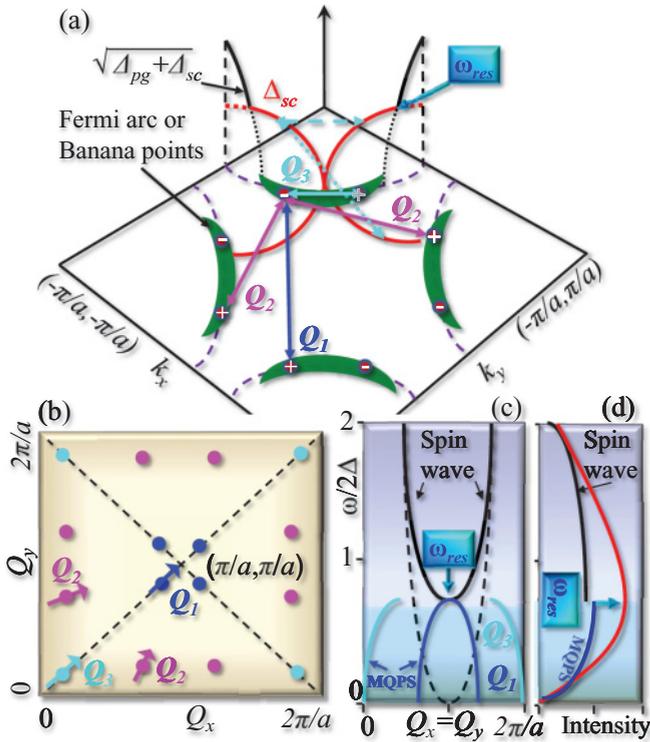
FIG. 1. (Color online) Origin of MQPS vectors. (a) Sketch of cuprate constant-energy cut, showing four "banana"-shaped regions (green shapes) with intense spectral features at their tips (red dots). The gap as a function of angle is shown on one banana (red and black lines). Above the Fermi pocket, the superconducting gap is cut off by a competing-order pseudogap (black solid line). On this gap curve the contrasting behavior of QPI and MQPS vectors is illustrated: The QPI vectors connect two banana tips at the same energy, as shown by the long-dashed cyan line, while the MQPS vectors connect banana tips across the Fermi energy, from an electron tip at $\omega < 0$ to a hole tip at $\omega > 0$, shown by the dotted cyan arrow for the Q_3 branch. For convenience the various MQPS vectors are defined by projected horizontal arrows, labeled Q_1–Q_3, illustrating the two bright points that they connect. (b) The q-space representation of the MQPS. Symbols represent the Q_i vectors of the same color as shown in (a). The associated arrows point in the direction that the Q_i vectors shift with increasing energy along the Fermi surface. (c) The energy and momentum dispersions of two Q_i vectors are shown along the diagonal direction ($Q_x = Q_y$). [The intensity of Q_3 is expected to be low (see text).] The black solid line depicts the spin waves which are gapped below the SC gap while the black dashed line stands for the gapless-spin-wave (schematic) dispersion expected in the non-superconducting state. (d) Both spin wave (solid black) and MQPS (solid blue) have monotonic intensity variation as a function of energy, and as they meet at Q, the total intensity (red line) attains a sharp peak.

inversion procedure performed using the QPI features in the STM spectra. Figure 1(a) depicts a typical form of the Fermi surface (green shadings) which is assumed to be truncated below the antiferromagnetic Brillouin zone due to the presence of underlying pseudogap ordering. When the superconducting gap has a d-wave form $\Delta_k = \Delta_0[\cos(k_x a) - \cos(k_y a)]/2$, where a is the in-plane lattice constant, the spectral function at any particular energy $\omega \leqslant 2\Delta_0$ has a maximal intensity at eight

bright points $K(\omega)$ that develop on four banana pockets which satisfy $\omega = \Delta_{K(\omega)}$ (red dots). In STM experiments, elastic scattering at energy ω is dominated by scattering between these points, leading to a form of Friedel oscillations known as QPI, satisfying the condition[1,2]

$$\omega = \Delta_{K(\omega)} = \Delta_{K(\omega)+q_i}. \tag{1}$$

The long-dashed cyan arrow in Fig. 1(a) illustrates one possible q_i vector.

Origin of MQPS. The INS experiments, which measure the imaginary part of the transverse spin-spin correlation function χ'', can also be understood through an analogy with the QPI pattern.[5,7] Indeed, since χ is related to the joint density of states (JDOS), the neutron scattering will be dominated by transitions from banana tips below the Fermi level to banana tips above the Fermi level, as illustrated by the dotted cyan arrow in Fig. 1(a). The energy of a particular transition will be given by

$$\omega(Q_i) = |\Delta_k| + |\Delta_{k+Q_i}| = \Delta_0[|g_k| + |g_{k+Q_i}|], \tag{2}$$

where the d-wave structure factor is $g_k = [\cos(k_x a) - \cos(k_y a)]/2$.

Similarity and differences between MQPS and QPI. While the same banana points contribute to both QPI and neutron scattering, there are actually more q vectors in the former case. In elastic scattering there are 7 q_i vectors at any energy that connect a given banana point to the other banana points.[1,2] However, in INS there is a coherence factor which allows only the poles for which Δ_k and Δ_{k+Q_i} have opposite signs, since the magnetic neutron scattering cross-section is odd under time-reversal symmetry.[5–7] Hence we identify three neutron scattering vectors which dominate in cuprates and give rise to a spin excitation profile, which can be called the MQPS pattern, in analogy with the QPI patterns. The MQPS vectors, shown in Fig. 1(a), can be denoted as $Q_{1,2,3} \sim q_{3,6,7}$ (we do not distinguish the QPI vectors q_2 and q_6 which have the same length, denoting both as Q_2), where the lowercase q's are the corresponding QPI vectors.[1,2]

There is a second, more important difference from QPI. Note that for fixed ω Eq. (1) is the equation of a point in q space, while Eq. (2) is the equation of a curve, because there will be a different Q_i for each pair Δ_k and Δ_{k+Q_i} which satisfy Eq. (2). However, we show below that this is not a problem: The gap and FS can be reconstructed from INS data along any Q-ω cut. INS data are mostly available along the diagonal cut $Q_x = Q_y$ and along the bond direction, i.e., $[(\pi,0) \to (\pi,2\pi)]$, and equivalent cuts as a function of energy. We therefore define the spanning vectors as Q_1 and Q_3 along the diagonal direction and Q_1' and Q_3' along the bond direction (note that Q_2 does not lie on these special cuts). The diagonal cut is a particularly simple choice, since along this cut the MQPS vectors are exclusively associated with special points, for which $\Delta_k = -\Delta_{k+Q_i}$. For these special points the analogy with QPI becomes exact, with $\omega_{\mathrm{MQPS}} = 2\omega_{\mathrm{QPI}}$. Along the bond direction, the situation is similar as discussed below.

The Q-space positions of the poles of Eq. (2), or the MQPS pattern, are plotted schematically at a constant energy in Fig. 1(b). The associated arrows indicate the direction each vector moves as the excitation energy increases which is determined by the shape of the Fermi pocket and the d-wave

superconducting gap values at each Fermi momentum, just as for QPI. To see this, we draw an illustrative energy versus momentum dispersion relation for the two Q_i vectors along the diagonal direction in Fig. 1(c). Branch Q_1 disperses from $\omega = 0$, where the incommensurate Q_1 vector connects pairs of nodal points, and hence measures the width of the hole pocket, to the resonance peak at (π,π) at energy $\omega = \omega_{\text{res}}$ connecting the hot spots at the boundary of the magnetic Brillouin zone—that is, Q_1 is the dispersion branch associated with the magnetic resonance peak. Branch Q_3 represents an intrapocket scattering, and the corresponding branch starts from $Q_3 = 0$, $\omega = 0$ at the nodal point, dispersing toward a Q_3 vector which spans the length of the hole pocket when $\omega = \omega_{\text{res}}$. Thus both curves attain the maximal ω when the banana points correspond to the hot spots along the Brillouin zone diagonals—the maximal diagonals of the hole pockets. A similar phenomenon is found in the experimental QPI spectra.[1,2] In summary, the inelastic MQPS intensity pattern at an energy $\omega = 2\Delta$ in neutron scattering exactly corresponds to the elastic QPI pattern seen at an energy $\omega = \Delta$ in STM, and hence can also be used to reconstruct the Fermi surface and SC gap properties.

III. MAGNETIC RESONANCE PEAK AND HOURGLASS DISPERSION

QP-GW model. To illustrate how the above results play out in practice, we compare them to experiment and to realistic calculations of INS. We calculate the INS spectrum of the cuprates from a one-band Hubbard model, with self-energy corrections from a *GW* calculation called the quasiparticle-GW (QP-GW) model.[19,20] The QP-GW Hamiltonian consists of four components which are calculated self-consistently: $H_{\text{LDA}} + H_{\text{SDW}} + H_{\text{SC}} + \Sigma$. The electronic dispersion, H_{LDA}, is based on a tight-binding fit to the material-specific first-principles single-band dispersion of the antibonding combination of Cu $d_{x^2-y^2}$ and O $p_{x/y}$ orbitals.[21] As in our earlier analysis of QPI,[22] the pseudogap state is treated as a spin-density wave (SDW), H_{SDW}, based on a Hubbard term in the Hamiltonian, which is treated using standard random-phase-approximation (RPA) theory.[23] Below T_c, d-wave SC order develops H_{SC} which couples naturally to the SDW state.[24] The resulting energy spectrum is $E(\mathbf{k}) = \sqrt{(E^s)^2(\mathbf{k}) + \Delta_{\mathbf{k}}^2}$, where the non-superconducting dispersions for both spin states are $E^s = \xi^+(\mathbf{k}) \pm E_0(\mathbf{k})$ [for $E_0^2 = \xi^-(\mathbf{k})^2 + G^2$, $\xi^{\pm}(\mathbf{k}) = [\xi(\mathbf{k}) + \xi(\mathbf{k} + \mathbf{Q})]/2$, $\xi(\mathbf{k})$ is the noninteracting band in the Bloch state, and G is the effective SDW gap which produces the pseudogap above the antiferromagnetic zone boundary]. The SDW gap causes a substantially reconstructed Fermi surface (FS) at low temperature as shown in Fig. 2(c). At low temperature the d-wave superconducting gap coexists with the SDW state. By fixing U and the pairing interaction V, to account for the experimental values of pseudogap and superconducting gap, respectively (see Table I), there are no free parameters in the susceptibility calculation. Finally, we calculate the self-energy due to the magnetic and charge excitations which renormalizes the overall dispersion by a momentum-independent mass renormalization.

Spin susceptibility. The full susceptibility is computed in all spin channels within the random-phase approximation (RPA).
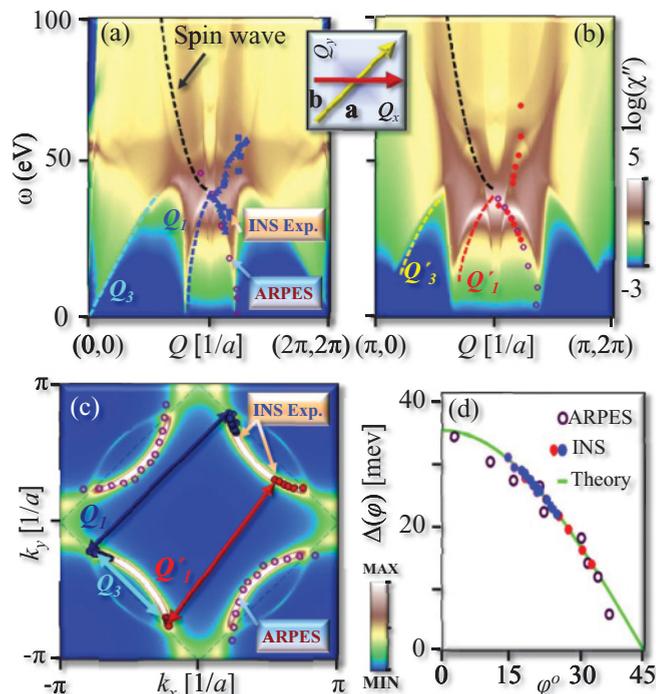
FIG. 2. (Color online) Reconstruction of Fermi surface from the INS spectra. (a), (b) Computed $\chi''(q,\omega)$ is plotted along the diagonal and bond directions, respectively (see inset), in the superconducting state of YBCO. The experimental data for YBCO$_{6+y}$ are shown in various symbols [green stars ($y = 0.85$) = Ref. 10, blue squares ($y = 0.85$) = Ref. 14, blue triangles ($y = 0.95$) = Ref. 26]. The data along the bond direction in (b) are obtained for $y = 0.6$ (red symbols) from Ref. 27. The blue and cyan dashed lines in (a) are the plot of Eq. (2) for Q_1 and Q_3 [red and yellow dashed lines are for corresponding equivalent vectors Q_1' and Q_3' along bond directions in (b)]. The brown symbols give the resonance spectrum calculated from Eq. (2) using ARPES dispersions (Ref. 28) for $y = 0.6$ as input [see (c)]. The experimental and theoretical lines are only plotted in one side of two equivalent directions for clarity. We plot $\chi''(q,\omega)$ in log scale to highlight weaker features. The black line is a guide to the eye for the dispersion expected for gapped spin waves, which constitutes the upward dispersion in the resonance spectrum. (c) Plot of computed Fermi surface of YBCO. The black symbols are the locus of the Fermi momenta determined from the experimental neutron data shown in (a) solving Eq. (2) while red symbols are the same but along the bond direction shown in (b). The brown symbols are the ARPES Fermi surface from Ref. 28. All symbols have fourfold symmetry, but are plotted here only along one particular quadrant for visualization. The blue and red arrows are the scattering vectors Q_1 and Q_1'. The light-blue arrow represents $Q_3(\omega_{\text{res}})$, which spans the length of the hole pocket. (d) The extracted superconducting gap is plotted as a function of Fermi surface angle [0° being the antinodal direction and 45° the nodal direction] from the neutron data of (a) and (b), compared to the ARPES data (brown symbols) of Ref. 29 and the present theoretical curve.

In RPA, the resonance pole is determined by the real part of the Lindhard susceptibility, χ_0', which has a logarithmic divergence at all the Bogoliubov quasiparticle scattering vectors. Simultaneously χ_0'' possesses a discontinuous jump due to the Kramers-Kronig relation. In this spirit, the positive divergence in χ_0' or the discontinuous jump in χ_0'' can be used

TABLE I. Order parameters of the model. Experimental gap values and the resulting self-consistent values of the order parameters. Given the order parameters, theoretical values of ω_{res} are calculated and compared with experiment. The value of U/t (where t is nearest-neighbor hopping parameter) is chosen to reproduce the experimental peudogap (Δ_{pg}) whose values are presented here along the "hot-spot" direction in the electron-doped case and the antinodal direction for all hole-doped cuprates. The value of U is in close agreement with our previous calculations (Refs. 19 and 41). Similarly, the parameter value of pairing potential V is taken to reproduce the superconducting gap (Δ), whose maximum value along the antinodal direction is presented here (Ref. 55). Our mean-field calculations overestimate the values of T_c, presumably due to the neglect of phase fluctuations (Ref. 37).

Material	Doping (x)	Δ_{pg} (meV) (Exp./Theory)	U/t (Theory)	Δ_{sc} (meV) (Exp./Theory)	Pairing Potential V (meV) (Theory)	T_c (K) Exp. (Theory)	ω_{res} Exp. (Theory)
NCCO	0.15	60 [Ref. 52]	4.1	3.5 [Ref. 53]	−26	24 (37) [Ref. 53]	4.5 (5) [Ref. 52]
YBCO$_{6.85}$	0.21	50 [Ref. 54]	2.5	35 [Ref. 26]	−98	92 (160) [Ref. 26]	41 (40) [Ref. 10]

as an indicator of the observed magnetic spectra in the SC state. In the SDW state, the situation is more complicated. Nevertheless, the overall phenomenology can be understood approximately from the imaginary part of the transverse spin susceptibility which mainly consists of three important factors (see Appendix A for more details):

$$\chi_0''(\boldsymbol{q},\omega) \approx \frac{\pi}{N} \sum_{\boldsymbol{k}} \sum A(\boldsymbol{k},\boldsymbol{q})C(\boldsymbol{k},\boldsymbol{q})\delta(\omega - \omega_{res}(\boldsymbol{k},\boldsymbol{q})). \quad (3)$$

Here, $\omega_{res}(\boldsymbol{k},\boldsymbol{q}) = E(\boldsymbol{k}) + E(\boldsymbol{k}+\boldsymbol{q})$, which converges to Eq. (2) on the Fermi surface [$E^s(\boldsymbol{k}) = 0$]. Since the INS spectrum is proportional to the RPA susceptibility χ'', the associated intensity of a given pole in the spectrum is controlled mainly by the two coherence factors A and C associated with antiferromagnetic zone folding and SC gap symmetry breaking, which can be approximated for the present discussion as

$$A(\boldsymbol{k},\boldsymbol{q}) = \frac{1}{2}\left(1 - \frac{\xi^-(\boldsymbol{k})\xi^-(\boldsymbol{k}+\boldsymbol{q}) + G^2}{E_0(\boldsymbol{k})E_0(\boldsymbol{k}+\boldsymbol{q})}\right), \quad (4)$$

$$C(\boldsymbol{k},\boldsymbol{q}) = \frac{1}{2}\left(1 - \frac{E^s(\boldsymbol{k})E^s(\boldsymbol{k}+\boldsymbol{q}) + \Delta_{\boldsymbol{k}}\Delta_{\boldsymbol{k}+\boldsymbol{q}}}{E(\boldsymbol{k})E(\boldsymbol{k}+\boldsymbol{q})}\right). \quad (5)$$

At the normal-state Fermi surface [$E^s(\boldsymbol{k}) = 0$], the superconducting coherence factor reduces to $C = 1/2[1 - \text{sgn}(g_{\boldsymbol{k}})\text{sgn}(g_{\boldsymbol{k}+\boldsymbol{q}})]$ which attains its maximum value of 1 whenever $\Delta_{\boldsymbol{k}}$ and $\Delta_{\boldsymbol{k}+\boldsymbol{q}}$ have opposite signs, thereby explaining why the spectrum is dominated by the three magnetic scattering channels Q_i with ($i = 1$–3). Furthermore, at small $|q - Q|$, the SDW coherence factor, Eq. (5), simplifies[25] to $A \rightarrow 1 - [\xi^-(\boldsymbol{k}) + \xi^-(\boldsymbol{k}+\boldsymbol{q})]G^2/4E_0^4(\boldsymbol{k}) = 1 - O((Q - q)^2)$, which attains its maximum value of 1 at $q = Q$. This explains why, since the Q_1 branch is closer to Q, its intensity dominates over the other branches and the intensity gradually increases to its maximum value at Q.

Upward and downward dispersion. Figure 2 presents our main result, showing that the dominant spectral features in neutron scattering correspond exactly to the MPQS features in a SDW superconductor. For a specific example we analyze YBa$_2$Cu$_3$O$_{6+y}$ (YBCO). The color plots in Figs. 2(a) and 2(b) show two-dimensional q-ω intensity maps of the calculated imaginary part of the RPA spin susceptibility (χ'') along the diagonal and the bond directions for YBCO at $y = 0.85$. Shown superimposed on the left side of Fig. 2(a) are the calculated MQPS dispersions, with $Q_1 = (\pi \pm \delta, \pi \pm \delta)$

plotted as a dashed blue line and $Q_3 = (\pm\delta, \pm\delta)$ as a dashed cyan line, computed from Eq. (2). Similarly, in Fig. 2(b) the dashed red [yellow] line represents the equivalent branch along the bond direction: $Q_1' = (\pi, \pi \pm \delta)/(\pi \pm \delta, \pi)$ [$Q_3' = (\pi, \pm\delta)/(\pm\delta, \pi)$]. We find good agreement with the experimental results, represented by symbols of various colors,[10,14,26,27] on the right-hand side of Figs. 2(a) and 2(b).

Along both momentum cuts an intense resonance feature is seen at (π,π), connecting to two oppositely dispersing branches at higher and lower energies. The downward branch is the MQPS branch in which Q_1 and Q_3 scatterings are observed. The upward branch has a different origin, related to the residual spin-density wave. At half filling, the upward spin-wave branch is linear and extends to a zero-energy Goldstone mode at $\boldsymbol{Q} = (\pi,\pi)$;[23] see Fig. 5(a). When superconductivity is turned on, this Goldstone mode acquires a gap $\omega < 2\Delta_0$, and the upward and downward dispersions coexist and meet at the resonance energy. Note that the upward-dispersing branch cannot be reproduced in a paramagnetic metallic state or in any other time-reversal symmetry-invariant ground state as discussed in Sec. V below.

Why does the bond direction obtain stronger intensity than the diagonal one? There are two main sources of intensity variation for each Q vector. As discussed earlier, the SDW coherence factor is strongly momentum dependent and reaches a maximum at $\boldsymbol{Q}$. Since branch Q_3 stops dispersing well before it reaches $\boldsymbol{Q}$, its intensity is relatively low while the Q_1 branch gains more intensity as it moves toward the resonance. The equivalent Q_1' (Q_3') branch along the bond direction in Fig. 2(b) has twice as large intensity as Q_1 (Q_3) in Fig. 2(a). This is due to an overall degeneracy factor. The scattering vectors $Q_{1,3}'$ have one commensurate direction and one incommensurate one while $Q_{1,3}$ are incommensurate along both x and y directions except at the resonance at $\boldsymbol{Q}$. Thus $Q_{1,3}'$ connect twice as many Fermi surface points as any other $Q_{1,3}$. As a result the intensity of the magnetic spectrum along the bond direction [in Fig. 2(b)] is twice as large as that along the diagonal direction [in Fig. 2(a)]. Therefore, below the resonance peak the intensity profile is rotated along the bond direction as shown in Fig. 3(a).

Extracting Fermi surface and gap information. Now, the hole-pocket Fermi surface and the d-wave superconducting pairing can be extracted from the INS data and vice versa. The lower branch of the experimental data which disperses downward from (Q,ω_{res}) is associated with the Q_1 scattering
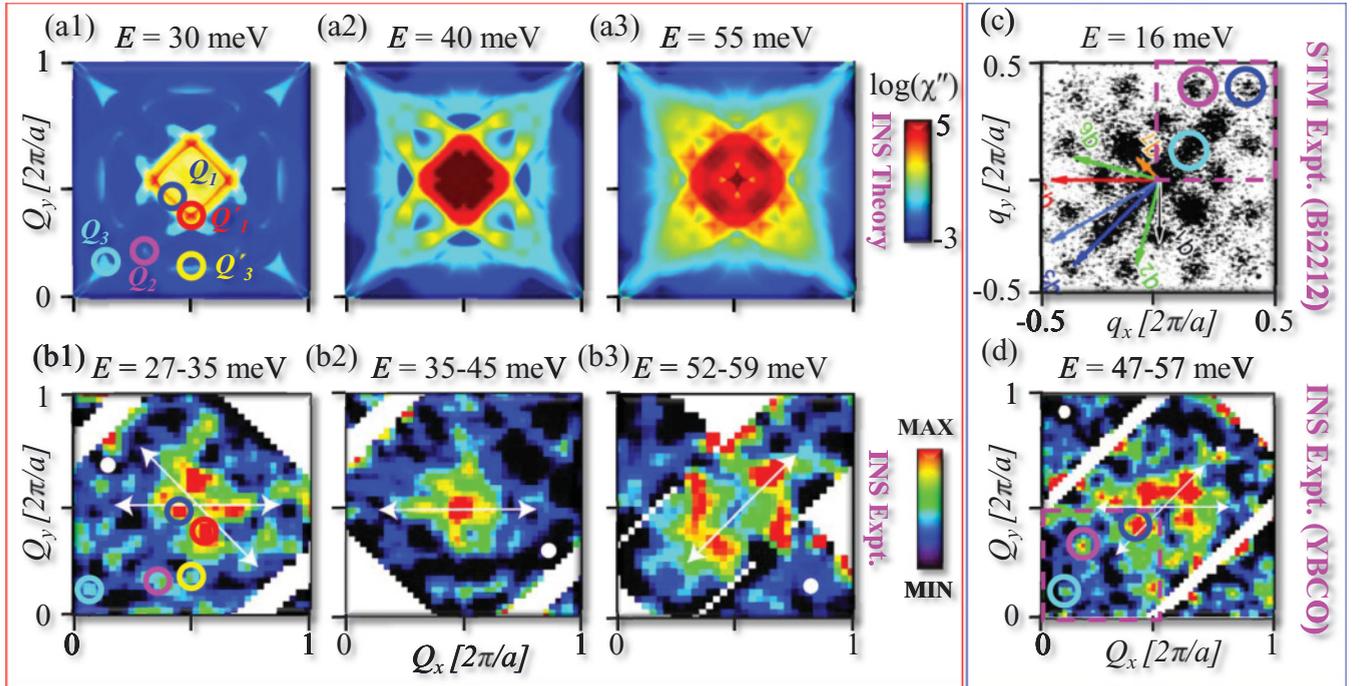
FIG. 3. (Color online) Comparison of MQPS maps with experimental QPI maps. (a1)–(a3) Computed spectra of $\chi''(\omega)$ are plotted in logarithmic scale for three representative constant-energy cuts, below the resonance, near the resonance, and above the resonance. (b1)–(b3) The corresponding experimental data of YBCO$_{6.95}$ from Ref. 13 for the acoustic channel, obtained after subtracting the corresponding normal-state data, which can enhance weak features away from Q. The white arrows in the experimental curves were used in the discussion in Ref. 13. (c) A QPI map of the STM data (Ref. 2) for Bi2212 is compared with the MQPS map of INS in (d). The MQPS spectrum is chosen in (d) for the optical channel to ease comparison with QPI maps as the magnetic profile is rotated here along the diagonal direction. We note that QPIs are usually plotted in the range $[-\pi$ to $\pi]$ while the neutron scattering is plotted in the range $[0$ to $2\pi]$; the dashed box in (c), (d) represents the range $[0$ to $\pi]$ to be compared. In (a1), (b1), and (d), circles of various colors depict various MQPS vectors while the circles with same colors in (c) are the corresponding QPI vectors.

vectors. Therefore, by solving Eq. (2) at the experimental points in Figs. 2(a) and 2(b), we determine a map of k_F (black and red dots) which agrees very well with the theoretical Fermi surface as well as with the ARPES FS in Fig. 2(c). Note that we find the same Fermi surface by utilizing the diagonal cut Q_1 [black dots in Fig. 2(c)] or the bond direction Q_1' [red dots]. The light blue arrow in Fig. 2(c) shows how Q_3 at ω_{res} can be used to determine the length of the hole pocket. Notably, recent studies have been able to extract weaker features from the INS data,[30] suggesting that determination of the remaining Q vectors may soon be possible. Alternatively, if the inversion is guided by a model calculation, the Q_1 vectors alone can provide valuable information about the pocket shape.

Reconstructing INS spectra from ARPES Fermi surface. For a cross-check, we use the experimental FS [brown open symbols in Fig. 2(c)] and gap measured by ARPES[28] to compute the magnetic resonance spectra by solving Eq. (2), brown open symbols in Fig. 2(a). This agrees well with the INS data. Furthermore, the extracted values of k_F versus ω can be used to determine the underlying superconducting gap symmetry using Eq. (2) which assumes $d_{x^2-y^2}$ symmetry. This also agrees well with ARPES data[29] and the present theory; see Fig. 2(d). The superconducting gap can be extracted up to the edge of the magnetic Brillouin zone or the hot spot ($\phi \sim 15°$), above which the pseudogap dominates in the spectrum and the MPQS features can no longer be followed.

IV. MQPS PATTERN AND COMPARISON WITH QPI PATTERN

MQPS versus QPI. Combining the MQPS and spin wave spectra, Fig. 3 compares the ω evolution of our present theoretical MQPS maps [Fig. 3(a)] with corresponding experimental data [Fig. 3(b)]. In the low-energy region, the magnetic scattering profile of Fig. 3(a1) has the highest intensity (red) along a square centered at (π,π). The intensity is larger along the bond directions than along the diagonal as discussed above, consistent with experiments shown in the corresponding lower panel. It should be noted that the experimental INS data plotted in Fig. 3 are obtained after subtracting out the normal-state contribution $[\chi''(15 \text{ K}) - \chi''(100 \text{ K})]$ to remove the background and enhance weaker features. This is why the MQPS pattern here looks much brighter than in other existing data sets. We note that there are hints of weak features corresponding to $Q_{2,3}$, although these are close to the noise level. The intensity variation in the equivalent Q points of the same Brillouin zone might be related to orbital form factors and other extrinsic effects, as observed, e.g., in ferroelectric materials.[31] Figure 3 also compares a QPI map (only available for Bi2212), in Fig. 3(c), with a neutron scattering map of the odd channel in YBCO, in Fig. 3(d). Again, there are hints of the three high-symmetry vectors $Q_{1,2,3}$ (and two equivalent vectors along the bond direction $Q_{1,2}'$) in Fig. 3(d) which

correspond to the $q_{3,6,7}$ vectors in the QPI map in Fig. 3(c) (denoted by circles of the same colors), but these features remain close to the noise level.

45° rotation of the spectra in going from MQPS to spin-wave dispersion. With increasing energy, at the resonance [Fig. 3(a2)] the intensity piles up at (π,π) with tails dispersing toward $q = (0,0)$ similar to what was recently seen in Hg-based compounds.[30] Above the resonance, Fig. 3(a3), the magnetic spectrum is purely spin-wave based and the profile is rotated along the diagonal direction, as found experimentally. In the above calculations, we have assumed that the superconductivity couples to the SDW order. When the spin-wave spectrum of upward dispersion and the MQPS of downward dispersion meet at the commensurate antiferromagnetic vector $Q = (\pi,\pi)$, a resonance peak in the intensity occurs. The SDW coherence factors play an important role in distributing the intensity over the entire magnetic spectrum, Eq. (4). Furthermore, the QPI-MQPS correspondence is obscured when the non-superconducting state becomes paramagnetic. While the Q_i vectors still play a significant role, the magnetic resonance peak is shifted to a lower energy at a pole of the dynamic susceptibility.[7] In the magnetic superconducting ground state, the susceptibility peaks correspond to the MQPS $Q_i(\omega)$, with ω given by Eq. (2), as shown in Figs. 2(a) and 2(b).

V. DISCUSSION AND CONCLUSIONS

Thus, we provide a simple explanation for the hourglass-shaped INS spectrum commonly seen in cuprates and other correlated materials.

The upward-dispersing branch is a signature of the competing order. Thus, models based on a pure superconducting phase with no competing order[5–7,32,33] are unable to explain this feature. Furthermore, if the competing phase is assumed to be a pure charge-density wave or d-density wave phase,[34] the corresponding Goldstone modes are not time-reversal symmetry breaking, and hence will not be able to account for the experimental observations. Furthermore, the time-reversal breaking orbital order phase will have a resonance peak concentrated at $\mathbf{q} = 0$[30,35] instead of the present $q = Q$ mode. On the other hand, if the competing order is magnetic, as in our SDW model but also in many models of stripes,[36] then the Goldstone modes are spin waves and so can explain the upper-branch dispersion. We note that since the dispersion starts at a finite frequency, it is not necessary that the competing order be long range, but only that there are significant short-range correlations. A demonstration that the competing order is magnetic is very significant, since a number of calculations have found that magnetic fluctuations can play an important role as the glue for high-T_c superconductivity.[37,38] The hourglass shape has also been observed in $La_{2-x}Ba_xCuO_4$, which has stripe order but only fluctuating superconductivity.[15] This suggests that there may be competing magnetic orders present.[39]

The resonance peak. The MQPS and spin wave both predict a gradual increase of intensity as one approaches the $\boldsymbol{Q}$ point, see Fig. 1(d), but neither acting alone can generate a true peak in the intensity, as has been demonstrated in earlier calculations.[5,6] In the present case of SDW + SC, we find that when the upward and downward dispersion of different origin meet at $\boldsymbol{Q}$, the intensity diverges and a true peak in the

intensity occurs, Fig. 4(c). In other words, the resonance peak represents the mass gap of the Goldstone mode of the phase competing with superconductivity within the present model.

The downward-dispersing branch can be used to recover the angle dependence of the superconducting gap and the underlying Fermi surface of the material when superconductivity is turned off. In contrast to the upper branch, this behavior is universal. Thus, if its resolution can be increased, INS stands poised to become a powerful tool for extracting important fundamental *bulk* information on many correlated systems of high current interest.

We note that our model of a combined SDW + d-wave SC ground state for the cuprates captures all three of the above key features of the spin excitation spectrum. The QP-GW model was designed to be the simplest model which could describe both intermediate-strength correlations and competing order in the cuprates. The INS results confirm that the leading competing order is strongly magnetic in nature. The most natural extension of the QP-GW model would thus seem to be one with an incommensurate competing order.[39] While the deeply underdoped regime could be the home of strikingly new physics,[40] we note that the QP-GW model has been quite successful in describing optical and ARPES spectra in this regime.[19,41]

Conclusions. In summary, we have shown that while a spin-wave spectrum of collective mode origin persists at all dopings both in electron- (in Appendix C) and hole-doped cuprates including at half filling, it becomes gapped in the low-energy region $\omega < 2\Delta$ where the spectrum is dominated by the Bogoliubov scatterings of Cooper pairs. When the spin-wave spectrum of upward dispersion and the magnetic scattering of downward dispersion meet at the commensurate antiferromagnetic vector Q, a resonance peak in the intensity occurs. INS spectroscopy is one of the few probes[42–44] which can be utilized to reconstruct the Fermi surface and superconducting properties of the actual bulk ground state. Our method of analysis is independent of any particular model and can be performed entirely from experimental inputs. Therefore, this inversion procedure can also be used to extract the bulk Fermi surface topology and pairing symmetry in newly discovered iron-selenide,[45,46] pnictide, chalcogenide,[47,48] and heavy-fermion[49–51] superconductors in which this information is still not settled. We also predict that the present formalism can be used to detect electron pockets on the cuprate Fermi surface, if they are present in the bulk ground state.

APPENDIX A: SUSCEPTIBILITY IN SDW + d-WAVE SC STATE

Since the SDW state causes a unit cell doubling, the correlation functions (Lindhard susceptibilities) are tensors

in momentum-space representation.[23] We define the susceptibilities as the standard linear response functions

$$\chi^{ij}(\boldsymbol{q},\boldsymbol{q}',\tau) = \frac{1}{2N}\langle T_\tau \Pi_{\boldsymbol{q}}^i(\tau)\Pi_{-\boldsymbol{q}'}^j(0)\rangle, \qquad (A1)$$

where the response operators (Π) for the charge and spin-density correlations respectively are

$$\rho_{\boldsymbol{q}}(\tau) = \sum_{\boldsymbol{k},\sigma} c_{\boldsymbol{k}+\boldsymbol{q},\sigma}^\dagger(\tau)c_{\boldsymbol{k},\sigma}(\tau),$$

$$S_{\boldsymbol{q}}^i(\tau) = \sum_{\boldsymbol{k},\sigma,\gamma} c_{\boldsymbol{k}+\boldsymbol{q},\sigma}^\dagger(\tau)\sigma_{\sigma,\gamma}^i c_{\boldsymbol{k},\gamma}(\tau). \qquad (A2)$$

The σ^i represent two-dimensional Pauli matrices along the ith direction and $c_{\boldsymbol{k},\sigma}$ ($c_{\boldsymbol{k},\sigma}^\dagger$) is the destruction (creation) operator of an electronic state at momentum $\boldsymbol{k}$ and spin σ. For transverse spin response $S^\pm = S_x \pm i S_y$ whereas longitudinal fluctuations are along the z direction only. In the present (π,π)-commensurate state, charge and longitudinal-spin fluctuations become coupled at finite doping. In common practice the transverse, longitudinal-spin, and charge susceptibilities are denoted as χ^{+-}, χ^{zz}, and χ^{00}, respectively. We collect all the terms into a single notation as $\chi^{\sigma\bar{\sigma}}$ where $\bar{\sigma} = \sigma$ gives the charge and longitudinal components and $\bar{\sigma} = -\sigma$ stands for the transverse component. For the pure SDW state Eq. (A1) can be evaluated rigorously. Here we generalize earlier calculations[23] for realistic cuprate band structures. For the combined SDW + d-wave SC state

$$\chi_{ij}^{\sigma\bar{\sigma}}(\boldsymbol{q},\omega) = \frac{1}{N\beta}\sum_{\boldsymbol{k},n,s} G_{is}(\boldsymbol{k},\sigma,i\omega_n)G_{sj}(\boldsymbol{k}+\boldsymbol{q},\bar{\sigma},i\omega_n+\omega) \qquad (A3)$$

$$= \frac{1}{N}\sideset{}{'}\sum_{\boldsymbol{k},\nu\nu'} A_{\nu\nu',ij}^{\sigma\bar{\sigma}}\sum_{m=1}^3 C_{\nu\nu'}^m \chi_{\nu\nu'}^m(\boldsymbol{k},\boldsymbol{q},\omega). \qquad (A4)$$

We obtain Eq. (A4) from Eq. (A3) after performing the Matsubara summation over n. G is the 4×4 single-particle Green's function in the Nambu space, constructed from the Hamiltonian given in the main text. The summation indices $\nu(\nu') = \pm$ refer to the two split SDW bands. Here, the coherence factor due to SDW order in the particle-hole channel is

$$A_{\nu\nu',11/22}^{\sigma\bar{\sigma}} = \frac{1}{2}\left(1 \pm \nu\nu' \frac{\xi_{\boldsymbol{k}}^- \xi_{\boldsymbol{k}+\boldsymbol{q}}^- + \sigma\bar{\sigma}(US)^2}{E_{0\boldsymbol{k}}E_{0\boldsymbol{k}+\boldsymbol{q}}}\right),$$

$$A_{\nu\nu',12/21}^{\sigma\bar{\sigma}} = -\nu\frac{G}{2}\left(\frac{\sigma}{E_{0\boldsymbol{k}}} + \nu\nu'\frac{\bar{\sigma}}{E_{0\boldsymbol{k}+\boldsymbol{q}}}\right). \qquad (A5)$$

The SC coherence factors are

$$C_{\nu\nu'}^1 = \frac{1}{2}\left(1 + \frac{E_{\boldsymbol{k}}^{s,\nu}E_{\boldsymbol{k}+\boldsymbol{q}}^{s,\nu'} + \Delta_{\boldsymbol{k}}\Delta_{\boldsymbol{k}+\boldsymbol{q}}}{E_{\boldsymbol{k}}^\nu E_{\boldsymbol{k}+\boldsymbol{q}}^{\nu'}}\right),$$

$$C_{\nu\nu'}^{2/3} = \frac{1}{4}\left(1 \pm \frac{E_{\boldsymbol{k}}^{s,\nu}}{E_{\boldsymbol{k}}^\nu} \mp \frac{E_{\boldsymbol{k}+\boldsymbol{q}}^{s,\nu'}}{E_{\boldsymbol{k}+\boldsymbol{q}}^{\nu'}} - \frac{E_{\boldsymbol{k}}^{s,\nu}E_{\boldsymbol{k}+\boldsymbol{q}}^{s,\nu'} + \Delta_{\boldsymbol{k}}\Delta_{\boldsymbol{k}+\boldsymbol{q}}}{E_{\boldsymbol{k}}^\nu E_{\boldsymbol{k}+\boldsymbol{q}}^{\nu'}}\right). \qquad (A6)$$

Lastly the index m represents the summation over three polarization bubbles related to the quasiparticle scattering ($m = 1$) and quasiparticle pair creation ($m = 2$) and pair annihilation ($m = 3$), as defined by

$$\chi_{\nu,\nu'}^1(\boldsymbol{k},\boldsymbol{q},\omega) = -\frac{f(E_{\boldsymbol{k}}^\nu) - f(E_{\boldsymbol{k}+\boldsymbol{q}}^{\nu'})}{\omega + i\delta + (E_{\boldsymbol{k}}^\nu - E_{\boldsymbol{k}+\boldsymbol{q}}^{\nu'})}, \qquad (A7)$$

$$\chi_{\nu,\nu'}^{2,3}(\boldsymbol{k},\boldsymbol{q},\omega) = \mp\frac{1 - f(E_{\boldsymbol{k}}^\nu) - f(E_{\boldsymbol{k}+\boldsymbol{q}}^{\nu'})}{\omega + i\delta \mp (E_{\boldsymbol{k}}^\nu + E_{\boldsymbol{k}+\boldsymbol{q}}^{\nu'})}. \qquad (A8)$$

In the RPA model, the 2×2 susceptibility is obtained from the standard formula[23]

$$\chi_{\mathrm{RPA},11}^{\sigma\bar{\sigma}}(\boldsymbol{q},\omega) = \frac{[1 + \sigma\bar{\sigma}U\chi_{22}^{\sigma\bar{\sigma}}(\boldsymbol{q},\omega)]\chi_{11}^{\sigma\bar{\sigma}}(\boldsymbol{q},\omega) + U[\chi_{12}^{\sigma\bar{\sigma}}(\boldsymbol{q},\omega)]^2}{[1 - U\chi_{11}^{\sigma\bar{\sigma}}(\boldsymbol{q},\omega)][1 + \sigma\bar{\sigma}U\chi_{22}^{\sigma\bar{\sigma}}(\boldsymbol{q},\omega)] + \sigma\bar{\sigma}[U\chi_{12}^{\sigma\bar{\sigma}}(\boldsymbol{q},\omega)]^2}, \qquad (A9)$$

$$\chi_{\mathrm{RPA},22}^{\sigma\bar{\sigma}}(\boldsymbol{q},\omega) = \frac{[1 - U\chi_{11}^{\sigma\bar{\sigma}}(\boldsymbol{q},\omega)]\chi_{22}^{\sigma\bar{\sigma}}(\boldsymbol{q},\omega) + U[\chi_{12}^{\sigma\bar{\sigma}}(\boldsymbol{q},\omega)]^2}{[1 - U\chi_{11}^{\sigma\bar{\sigma}}(\boldsymbol{q},\omega)][1 + \sigma\bar{\sigma}U\chi_{22}^{\sigma\bar{\sigma}}(\boldsymbol{q},\omega)] + \sigma\bar{\sigma}[U\chi_{12}^{\sigma\bar{\sigma}}(\boldsymbol{q},\omega)]^2}, \qquad (A10)$$

$$\chi_{\mathrm{RPA},12/21}^{\sigma\bar{\sigma}}(\boldsymbol{q},\omega) = \frac{\chi_{12}^{\sigma\bar{\sigma}}(\boldsymbol{q},\omega)}{[1 - U\chi_{11}^{\sigma\bar{\sigma}}(\boldsymbol{q},\omega)][1 + \sigma\bar{\sigma}U\chi_{22}^{\sigma\bar{\sigma}}(\boldsymbol{q},\omega)] + \sigma\bar{\sigma}[U\chi_{12}^{\sigma\bar{\sigma}}(\boldsymbol{q},\omega)]^2}. \qquad (A11)$$

In the longitudinal and charge channel ($\bar{\sigma} = \sigma$), the RPA corrections do not introduce any pole and thus all the normal structure lies above the charge gap in the particle-hole continuum. Along the transverse direction ($\bar{\sigma} = -\sigma$), a linear spin-wave dispersion develops in the normal state which extends to zero energy at $Q = (\pi,\pi)$.[23] The necessary condition to yield a gapless Goldstone mode is that Eqs. (A9)–(A11) reduce to the self-consistent SDW order parameter G at $q = Q$, which is indeed the case in the normal state.

In the SC state, this zero-energy spin wave shifts to $\omega = |\Delta_{\boldsymbol{k}_F}| + |\Delta_{\boldsymbol{k}_F+\boldsymbol{q}}|$, due to the particle-particle (and hole-hole)

scattering terms $\chi^{2,3}$ in Eq. (A8). These terms have finite intensity only if the SC gap changes sign at the "hot spot" $\boldsymbol{q}$,[5] see Eq. (A6). Above the SC gap, the spin-wave term coming from Eq. (A7) is turned on. The crossover between them creates the hourglass pattern presented in Fig. 2.

APPENDIX B: MECHANISM OF MQPS

The result shown in Fig. 2 of the main text is obtained from a coexisting state of SDW and d-wave SC order within the RPA framework. To understand the origin of the observed resonance
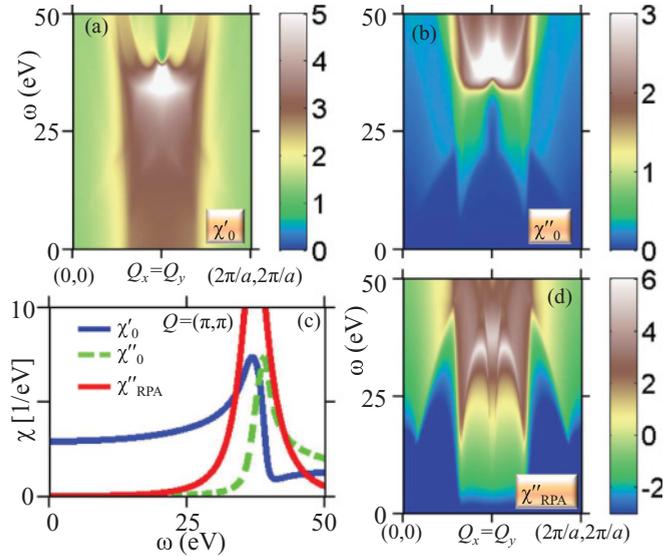
FIG. 4. (Color online) The real and imaginary part of bare susceptibility χ_0 is shown in (a) and (b), respectively, for YBCO. (c) All three susceptibilities are shown at the commensurate momentum cut. (d) Corresponding RPA result plotted in a logarithmic intensity scale as in the case of Fig. 2 of the main text.

FIG. 5. (Color online) INS calculations for electron-doped NCCO. (a) The spin-wave dispersion in the normal state at $x = 0$ in electron-doped NCCO along the diagonal direction compared with experimental data for LCO. (b) The INS spectrum for optimally doped NCCO. The theoretical spectrum is compared with the available experimental data of another electron-doped compound PLCCO at the latter's optimal doping. Due to the small superconducting gap, the resonance energy is much lower in the electron-doped case [arrow in the inset in (b)]. The incommensurate magnetic dispersion branches extending to zero energy are MQPS scattering associated with a hole pocket which develops near the magnetic quantum phase transition.

behavior, we decompose the resonance spectra of Fig. 2(b) into its bare components as shown in Fig. 4. Figures 4(a) and 4(b) show the real and imaginary parts of the bare susceptibility, which are related to each other by the Kramers-Kronig relation. Where the real part obtains a logarithmic divergence [blue line in Fig. 4(c)] the corresponding imaginary part possesses a discontinuous jump at the same location [green dashed line in Fig. 4(c)]. Within RPA, a resonance is possible when the condition $\chi_0' = 1/U$ is satisfied. In the region where χ_0' is greater than zero and also attains a divergence, a resonance can occur for a large range of U. In this spirit, a true resonance spectrum within RPA can simply be identified by tracing the divergences in χ_0' or by tracking the sudden peaks in χ_0''. We emphasize that this argument holds even for multiband pnictide superconductors.[48]

APPENDIX C: MAGNETIC RESONANCE SPECTRA IN ELECTRON-DOPED CUPRATE

Our analysis works equally well for other cuprates, but with strong band-structure-related modifications. Here we illustrate some issues in an electron-doped cuprate, NCCO, using the parameters from Table I. In Fig. 5(a), we show that the model well reproduces the experimental spin-wave spectrum of the undoped material, with a characteristic dispersion

$\omega(\mathbf{q}) \sim |\mathbf{Q} - \mathbf{q}|$, as depicted by the black line. Since the SC gap is much smaller, the resonance peak falls at a much lower energy, but this is still well captured by theory, Fig. 5(b). Note that the resonance peak is gapped, but has a spin-wave branch dispersing to higher energies. MQPS dispersions play an interesting role in the incommensurate branches of excitations which extend to $\omega = 0$. They are associated not with the main electron pockets, but with a subsidiary hole pocket that opens close to the SDW quantum critical point.

Something similar happens in hole-doped cuprates, where as doping increases toward the quantum critical point of the SDW state (which occurs slightly above optimal doping), electron pockets begin to form at the antinodal points. These new pockets have their own QPI, with associated banana points at energies higher than the Q resonance. Neutron scattering experiments should also be able to detect these electron pockets, which may be observed in quantum oscillation experiments. We also note that in a paramagnetic ground state, the magnetic scattering of the superconducting pairs survives above the resonance at all dopings and thus the model fails to explain the hourglass features, and predicts other spurious resonance energy scales which are not observed in experiments.

[1] T. Hanaguri, Y. Kohsaka, J. C. Davis, C. Lupien, I. Yamada, M. Azuma, M. Takano, K. Ohishi, M. Ono, and H. Takagi, Nature Phys. **3**, 865 (2007).

[2] Y. Kohsaka, C. Taylor, P. Wahl, A. Schmidt, J. Lee, K. Fujita, J. W. Alldredge, K. McElroy, J. Lee, H. Eisaki, S. Uchida, D.-H. Lee, and J. C. Davis, Nature (London) **454**, 1072 (2008).

[3] A. Bansil and M. Lindroos, Phys. Rev. Lett. **83**, 5154 (1999); A. Bansil, M. Lindroos, S. Sahrakorpi, and R.S. Markiewicz, Phys. Rev. B **71**, 012503 (2005).

[4] J. Nieminen, H. Lin, R. S. Markiewicz, and A. Bansil, Phys. Rev. Lett. **102**, 037001 (2009); J. Nieminen, I. Suominen, R. S. Markiewicz, H. Lin, and A. Bansil, Phys. Rev. B **80**, 134509 (2009).

[5] Ar. Abanov and A. V. Chubukov, Phys. Rev. Lett. **83**, 1652 (1999).

[6]M. Eschrig and M. R. Norman, Phys. Rev. B **67**, 144503 (2003).

[7]I. Eremin, D. K. Morr, A. V. Chubukov, K. H. Bennemann, and M. R. Norman, Phys. Rev. Lett. **94**, 147001 (2005).

[8]S. D. Wilson, P. Dai, S. Li, S. Chi, H. J. Kang, and J. W. Lynn, Nature (London) **442**, 59 (2006).

[9]B. Vignolle, S. M. Hayden, D. F. McMorrow, H. M. Ronnow, B. Lake, C. D. Frost, and T. G. Perring, Nature Phys. **3**, 163 (2007).

[10]P. Bourges, Y. Sidis, H. F. Fong, L. P. Regnault, J. Bossy, A. Ivanov, and B. Keimer, Science **288**, 1234 (2000).

[11]S. M. Hayden, H. A. Mook, P. Dai, T. G. Perring, and F. Dogan, Nature (London) **429**, 531 (2004).

[12]H. F. Fong, P. Bourges, Y. Sidis, L. P. Regnault, A. Ivanov, G. D. Guk, N. Koshizuka, and B. Keimer, Nature (London) **398**, 588 (1999).

[13]H. Woo, P. Dai, S. M. Hayden, H. A. Mook, T. Dahm, D. J. Scalapino, T. G. Perring, and F. Doan, Nature Phys. **2**, 600 (2006).

[14]S. Pailhés, Y. Sidis, P. Bourges, V. Hinkov, A. Ivanov, C. Ulrich, L. P. Regnault, and B. Keimer, Phys. Rev. Lett. **93**, 167001 (2004).

[15]J. M. Tranquada, H. Woo, T. G. Perring, H. Goka, G. D. Gu, G. Xu, M. Fujita, and K. Yamada, Nature (London) **429**, 534 (2004).

[16]P. Dai, H. A. Mook, R. D. Hunt, and F. Dogan, Phys. Rev. B **63**, 054525 (2001).

[17]G. Yu, Y. Li, E. M. Motoyama, and M. Greven, Nature Phys. **5**, 873 (2009).

[18]As stressed by Yu *et al*. (Ref. 17), Δ_{SC} is the SC gap, and does not include the pseudogap.

[19]T. Das, R. S. Markiewicz, and A. Bansil, Phys. Rev. B **81**, 174504 (2010).

[20]T. Das, R. S. Markiewicz, and A. Bansil, Phys. Rev. B **81**, 184515 (2010).

[21]R. S. Markiewicz, S. Sahrakorpi, M. Lindroos, Hsin Lin, and A. Bansil, Phys. Rev. B **72**, 054519 (2005).

[22]Tanmoy Das, R. S. Markiewicz, and A. Bansil, Phys. Rev. B **77**, 134516 (2008).

[23]J. R. Schrieffer, X. G. Wen, and S.-C. Zhang, Phys. Rev. B **39**, 11663 (1989).

[24]T. Das, R. S. Markiewicz, and A. Bansil, Phys. Rev. Lett. **98**, 197004 (2007).

[25]S. Sachdev, A.V. Chubukov, and A. Sokol, Phys. Rev. B **51**, 14874 (1995).

[26]D. Reznik, J.-P. Ismer, I. Eremin, L. Pintschovius, T. Wolf, M. Arai, Y. Endoh, T. Masui, and S. Tajima, Phys. Rev. B **78**, 132503 (2008).

[27]V. Hinkov, B. Keimer, A. Ivanov, P. Bourges, Y. Sidis, and C. D. Frost, New J. Phys. **12**, 105006 (2010).

[28]H. Yagi, T. Yoshida, A. Fujimori, K. Tanaka, N. Mannella, W. L. Yang, X. J. Zhou, D. H. Lu, Z.-X. Shen, Z. Hussain, M. Kubota, K. Ono, Y. Segawa, Y. Ando, D. Iijima, M. Goto, K. M. Kojima, and S. Uchida, e-print arXiv:1002.0655.

[29]K. Nakayama, T. Sato, K. Terashima, H. Matsui, T. Takahashi, M. Kubota, K. Ono, T. Nishizaki, Y. Takahashi, and N. Kobayashi, Phys. Rev. B **75**, 014513 (2007).

[30]L. Yuan, V. Balédent, G. Yu, N. Barisic, K. Hradil, R. A. Mole, Y. Sidis, P. Steffens, X. Zhao, P. Bourges, and M. Greven, Nature (London) **468**, 283 (2010).

[31]M. Frontzek, J. T. Haraldsen, A. Podlesnyak, M. Matsuda, A. D. Christianson, R. S. Fishman, A. S. Sefat, Y. Qiu, J. R. D. Copley, S. Barilo, S. V. Shiryaev, and G. Ehlers, Phys. Rev. B **84**, 094448 (2011).

[32]D. S. Inosov, S. V. Borisenko, I. Eremin, A. A. Kordyuk, V. B. Zabolotnyy, J. Geck, A. Koitzsch, J. Fink, M. Knupfer, B. Büchner, H. Berger, and R. Follath, Phys. Rev. B **75**, 172505 (2007).

[33]I. Eremin, D. K. Morr, A. V. Chubukov, and K. Bennemann, Phys. Rev. B **75**, 184534 (2007).

[34]J.-P. Ismer, I. Eremin, and Dirk K. Morr, Phys. Rev. B **73**, 104519 (2006).

[35]Yan He and C. M. Varma, Phys. Rev. Lett. **106**, 147001 (2011).

[36]M. Vojta and T. Ulbricht, Phys. Rev. Lett. **93**, 127002 (2004); G. Seibold and J. Lorenzana, *ibid*. **94**, 107006 (2005); J. M. Tranquada, H. Woo, T. G. Perring, H. Goka, G. D. Gu, G. Xu, M. Fujita, and K. Yamada, J. Phys. Chem. Solids **67**, 511 (2006).

[37]R. S. Markiewicz and A. Bansil, Phys. Rev. B **78**, 134513 (2008).

[38]T. Dahm, V. Hinkov, S. V. Borisenko, A. A. Kordyuk, V. B. Zabolotnyy, J. Fink, B. Büchner, D. J. Scalapino, W. Hanke, and B. Keimer, Nature Phys. **5**, 217 (2009).

[39]R. S. Markiewicz, J. Lorenzana, G. Seibold, and A. Bansil, Phys. Rev. B **81**, 014509 (2010).

[40]P. A. Lee, N. Nagaosa, and X.-G. Wen, Rev. Mod. Phys. **78**, 17 (2006); E. Demler and S.-C. Zhang, Phys. Rev. Lett. **75**, 4126 (1995).

[41]C. Kusko, R. S. Markiewicz, M. Lindroos, and A. Bansil, Phys. Rev. B **66**, 140513 (2002).

[42]The inelastic light scattering[43] and positron annihilation[44] are also bulk electronic structure probes.

[43]Y. Tanaka, Y. Sakurai, A. T. Stewart, N. Shiotani, P. E. Mijnarends, S. Kaprzyk, and A. Bansil, Phys. Rev. B **63**, 045120 (2001); S. Huotari, K. Hamalinen, S. Manninen, S. Kaprzyk, A. Bansil, W. Caliebe, T. Buslaps, V. Honkimaki, and P. Suortti, *ibid*. **62**, 7956 (2000).

[44]L. C. Smedskjaer, A. Bansil, U. Welp, Y. Fang, and K. G. Bailey, J. Phys. Chem. Solids **52**, 1541 (1991); P. E. Mijnarends, A. C. Kruseman, A. van Veen, H. Schut, and A. Bansil, J. Phys.: Condens. Matter **10**, 10383 (1998).

[45]T. Das and A. V. Balatsky, Phys. Rev. B **84**, 014521 (2011).

[46]T. Das and A. V. Balatsky, Phys. Rev. B **84**, 115117 (2011).

[47]D. N. Argyriou, A. Hiess, A. Akbari, I. Eremin, M. M. Korshunov, J. Hu, B. Qian, Z. Mao, Y. Qiu, C. Broholm, and W. Bao, Phys. Rev. B **81**, 220503(R) (2010), and the references therein.

[48]T. Das and A. V. Balatsky, Phys. Rev. Lett. **106**, 157004 (2011).

[49]O. Stockert, J. Arndt, E. Faulhaber, C. Geibel, H. S. Jeevan, S. Kirchner, M. Loewenhaupt, K. Schmalzl, W. Schmidt, Q. Si, and F. Steglich, Nature Phys. **7**, 119 (2011).

[50]C. Stock, C. Broholm, J. Hudis, H. J. Kang, and C. Petrovic, Phys. Rev. Lett. **100**, 087001 (2008).

[51]T. Das, J.-X. Zhu, and M. J. Graf, Phys. Rev. Lett. **108**, 017001 (2012).

[52]G. Yu, Y. Li, E. M. Motoyama, R. A. Hradil, R. A. Mole, and M. Greven, e-print arXiv:0803.3250.

[53]M. M. Qazilbash, A. Koitzsch, B. S. Dennis, A. Gozar, H. Balci, C. A. Kendziora, R. L. Greene, and G. Blumberg, Phys. Rev. B **72**, 214510 (2005).

[54]S. Huefner, M. A. Hossain, A. Damascelli, and G. A. Sawatzky, Rep. Prog. Phys. **71**, 062501 (2008).

[55]T. Das, R. S. Markiewicz, and A. Bansil, Phys. Rev. B **74**, 020506 (2006).